A&A 440, 151–161 (2005)
DOI: 10.1051/0004-6361:20041836

Astronomy & Astrophysics

Star formation in Perseus

Clusters, filaments and the conditions for star formation⋆

J. Hatchell[1,2], J. S. Richer[3], G. A. Fuller[4], C. J. Qualtrough[3], E. F. Ladd[5], and C. J. Chandler[6]

[1] Max-Planck-Institut für Radioastronomie, Auf dem Hügel 69, 53121 Bonn, Germany
e-mail: hatchell@astro.ex.ac.uk
[2] School of Physics, University of Exeter, Stocker Road, Exeter EX4 4QL, UK
[3] Cavendish Laboratory, Madingley Road, Cambridge CB3 0HE, UK
[4] Department of Physics, UMIST, PO Box 88, Manchester M60 1QD, UK
[5] Department of Physics, Bucknell University, Lewisburg, PA 17837, USA
[6] National Radio Astronomy Observatory, PO Box O, Socorro, NM 87801, USA

Received 12 August 2004 / Accepted 4 May 2005

Abstract. We present a complete survey of current star formation in the Perseus molecular cloud, made at 850 and 450 μm with SCUBA at the JCMT. Covering 3 deg^2, this submillimetre continuum survey for protostellar activity is second in size only to that of ρ Ophiuchus (Johnstone et al. 2004, ApJ, 611, L45). Complete above 0.4 $M_\odot$ (5σ detection in a 14″ beam), we detect a total of 91 protostars and prestellar cores. Of these, 80% lie in clusters, representative of star formation across the Galaxy. Two of the groups of cores are associated with the young stellar clusters IC 348 and NGC 1333, and are consistent with a steady or reduced star formation rate in the last 0.5 Myr, but not an increasing one. In Perseus, 40–60% of cores are in small clusters (<50 $M_\odot$) and isolated objects, much more than the 10% suggested from infrared studies. Complementing the dust continuum, we present a C^{18}O map of the whole cloud at 1′ resolution. The gas and dust show filamentary structure of the dense gas on large and small scales, with the high column density filaments breaking up into clusters of cores. The filament mass per unit length is 5–11 $M_\odot$ per 0.1 pc. Given these filament masses, there is no requirement for substantial large scale flows along or onto the filaments in order to gather sufficient material for star formation. We find that the probability of finding a submillimetre core is a strongly increasing function of column density, as measured by C^{18}O integrated intensity, $P(\mathrm{core}) \propto I^{3.0}$. This power law relation holds down to low column density, suggesting that there is no A_v threshold for star formation in Perseus, unless all the low-A_v submm cores can be demonstrated to be older protostars which have begun to lose their natal molecular cloud.

Key words. stars: formation – submillimeter – dust, extinction – ISM: molecules – ISM: clouds – ISM: structure

1. Introduction

Recent advances in submillimetre (submm) detector technology now make it possible to image entire star forming regions and detect all the protostellar and starless cores within. For the first time, we can gather statistically significant samples of stars at the earliest stages of their evolution. At the same time, theories of star formation are moving on from the formation of individual, isolated objects (e.g., Shu et al. 1987) to the formation of clusters (e.g., Mac Low & Klessen 2004). It is thus hugely important at this time to make large surveys of star formation regions to compare with the theories.

An important question which we can only address with submm surveys is where in molecular clouds stars form. This cannot be answered by looking at older populations of pre-main-sequence stars detectable in the infrared and optical because the typical velocities of the stars lead them to wander by 1 pc/Myr, and the environment in which they formed may no longer exist. Therefore we are driven to look for stars at the point of formation or shortly after, at protostellar cores and deeply embedded Class 0 objects, with ages less than or of order 10^4 years. With submm surveys we can relate the positions of the young protostars to the properties of the dust and gas in the molecular clouds in which they form. This has led other authors (Onishi et al. 1998; Johnstone et al. 2004) to conclude that there is an extinction or column density threshold for star formation, that is, that stars only form in the densest parts of molecular clouds. We investigate this conclusion further in this paper.

We have carried out a complete survey of star formation above 0.4 $M_\odot$ in the Perseus molecular cloud. Perseus was selected as it is known to be forming clusters of stars and more massive stars than, e.g., Taurus. The Perseus molecular cloud contains a total of 17 000 $M_\odot$ of gas, estimated from visual extinction (Bachiller & Cernicharo 1986b). Our survey area of ∼3 deg^2 was selected to include all the moderate to high extinction material ($A_\mathrm{v} > 4$) where star formation

⋆ Appendix is only available in electronic form at
http://www.edpsciences.org

might occur. Imaging dust emission at 850 and 450 μm with the Submillimetre Common User Bolometer Array (SCUBA) at the James Clerk Maxwell Telescope (JCMT), we detect all the protostars and starless cores above 0.4 $M_\odot$/14″ beam. Complementing the dust continuum images, we present molecular line ($C^{18}O$ J = 1–0) data at 1′ resolution. Thus, we can relate the star formation activity to the underlying physical properties of the molecular cloud and to the kinematics. By imaging a single molecular cloud we minimise the uncertainties in derived masses, sizes, etc., due to distance.

The Perseus molecular cloud is a well known star forming cloud in the nearby Galaxy. It is associated with two clusters containing pre-main-sequence stars: IC 348, with an estimated age of 2 Myr (and spread of ±1.5 Myr; Luhman et al. 2003); NGC 1333, which is less than 1 Myr in age (Lada et al. 1996; Wilking et al. 2004); and the Per 0B2 association, which contains a B0.5 star (Steenbrugge et al. 2003) and therefore must be less than 13 Myr in age (Meynet & Maeder 2000). These clusters therefore all show evidence of star formation activity within the last $\sim 10^7$ years. The molecular cloud itself contains a number of previously known protoclusters and isolated protostars but until now there has been no complete census of the current star formation activity.

We assume the distance to the Perseus molecular cloud to be the same as the Hipparcos distance to the embedded clusters, and use 320 pc throughout (de Zeeuw et al. 1999).

2. Observations and data reduction

Images of Perseus were obtained at 850 and 450 μm using SCUBA on the JCMT during 20 nights between 1999 and 2003. The region selected corresponds roughly to the $\int T_A^* \, dV = 4$ K km s^{-1} contour of the Bell labs 7m ^{13}CO map[1], although not all of this area was mapped with both SCUBA and $C^{18}O$, while some regions outside this contour were mapped with each. For completeness and calibration consistency we included the NGC 1333 region although it was mapped previously with SCUBA by Sandell & Knee (2001). The whole region covered contains more than 10 000 $M_\odot$ of gas, estimated from ^{13}CO. Fields of size 10′ × 10′ were scan-mapped 6 times with each of 3 chop throws (30″, 44″ and 68″) and 2 chop directions (RA and Dec). The data were reduced using SURF (Jenness & Lightfoot 1998). The typical rms noise level is 35 mJy/beam at 850 μm. The weather conditions for the 450 μm observations were more variable: for the clusters (observed in the best conditions as we expected to find sources here) the noise level is ~200 mJy/beam, but increases to >1 Jy/beam in other regions. The 450 and 850 μm beam sizes are 8″ and 14″ respectively or 0.012 and 0.022 pc at the distance of Perseus. We assume a dust emissivity of $\kappa_{850} = 0.012$ cm^2 g^{-1} (gas+dust), from Ossenkopf & Henning (1994) model 5 for icy coagulated grains and a gas-to-dust mass ratio of 161 (1.5×10^{-26} g of dust per H atom; Draine & Lee 1984), assuming gas is 0.89% H by number (Churchwell et al. 1990). Our beam mass sensitivity to a 12 K core is then 0.4 $M_\odot$ at 850 μm, although we also detect warmer, less massive objects, and our beam-averaged column density sensitivity is 6×10^{22} cm^{-2} (both limits given for 5σ detections).

Maps of the molecular cloud in $C^{18}O$ J = 1–0 were made in January and December 2000 using the 4×4 array SEQUOIA on the FCRAO 14 m telescope. The beamsize was 46″, corresponding to 0.07 pc at the distance of Perseus. The 92 500 spectra were baselined, calibrated to T_{MB} with an efficiency of 0.45, smoothed to 0.25 km s^{-1} resolution, gridded and integrated in velocity over 0–12 km s^{-1} using the GILDAS software, to produce the integrated intensity map shown in Fig. 1. Visualisation and further analysis of the $C^{18}O$ were carried out using the Karma visualisation suite (Gooch 1996). Maps of ^{13}CO(1–0) were also obtained during this same observing period, the results from which will be presented at a later date.

We take $N(C^{18}O) = 3.4 \times 10^{14}(A_v - 1.6)$ cm^{-2} (Bachiller & Cernicharo 1986b), or alternatively, $I(C^{18}O) = (A_v - 1.6)/3.6$ K km s^{-1}, assuming LTE at 12 K. We also assume $N(H+2H_2) = 0.9 \times 10^{20} A_v$ (Bohlin et al. 1978). The temperature of the molecular gas is typically 10–12 K from NH_3 observations (Bachiller & Cernicharo 1986a), although protostellar cores are warmer (30–50 K: Motte & André 2001; Jennings et al. 1987).

Our definition of a core for the purposes of this paper is a flux peak with closed contours at the 500, 250 or 150 mJy (~4σ) levels. Elongated regions at those levels were divided into subpeaks at subsidiary maxima. It should be borne in mind that it is not necessarily straightforward to convert our observational sensitivity of 0.4 $M_\odot$/beam to the minimum total mass of a core identifiable in our survey as this limit depends on the core density distribution and size: massive but extended cores could easily remain undetected. As a consequence it is likely we are least sensitive to the youngest and hence least centrally condensed prestellar cores. In addition if the pressure external to a core determines its size for a given mass, our core mass sensitivity may vary from region to region in the cloud giving a higher limit in the lower pressure regions away from the clusters (Johnstone et al. 2004). We are also insensitive to weak sources in the emission wings of strong ones and therefore underestimate the number of weak sources in clusters, an effect which is discussed further in the next section.

3. Clusters

The complete 850 μm image in Fig. 1 shows emission from dust cores and high column density gas. In many cases the cores already show central concentration indicative of gravitational collapse, and must be associated with the earliest stages of star formation.

We detect 91 dust cores with an 850 μm flux above 150 mJy/beam (>4σ detections). These are listed in Table A.1. About half of these are new submm detections. We see from Fig. 1 that most of the cores lie in five main groups: from east to west in the cloud, the HH211 region, B1, NGC 1333, L1455 and L1448. Additionally, there are a few scattered isolated cores and two cores in B5. These groups are shown in

[1] The ^{13}CO map is available from John Bally, at `http://casa.Colorado.EDU/~bally/ftp/7mdata/Perseus_13co.fits`

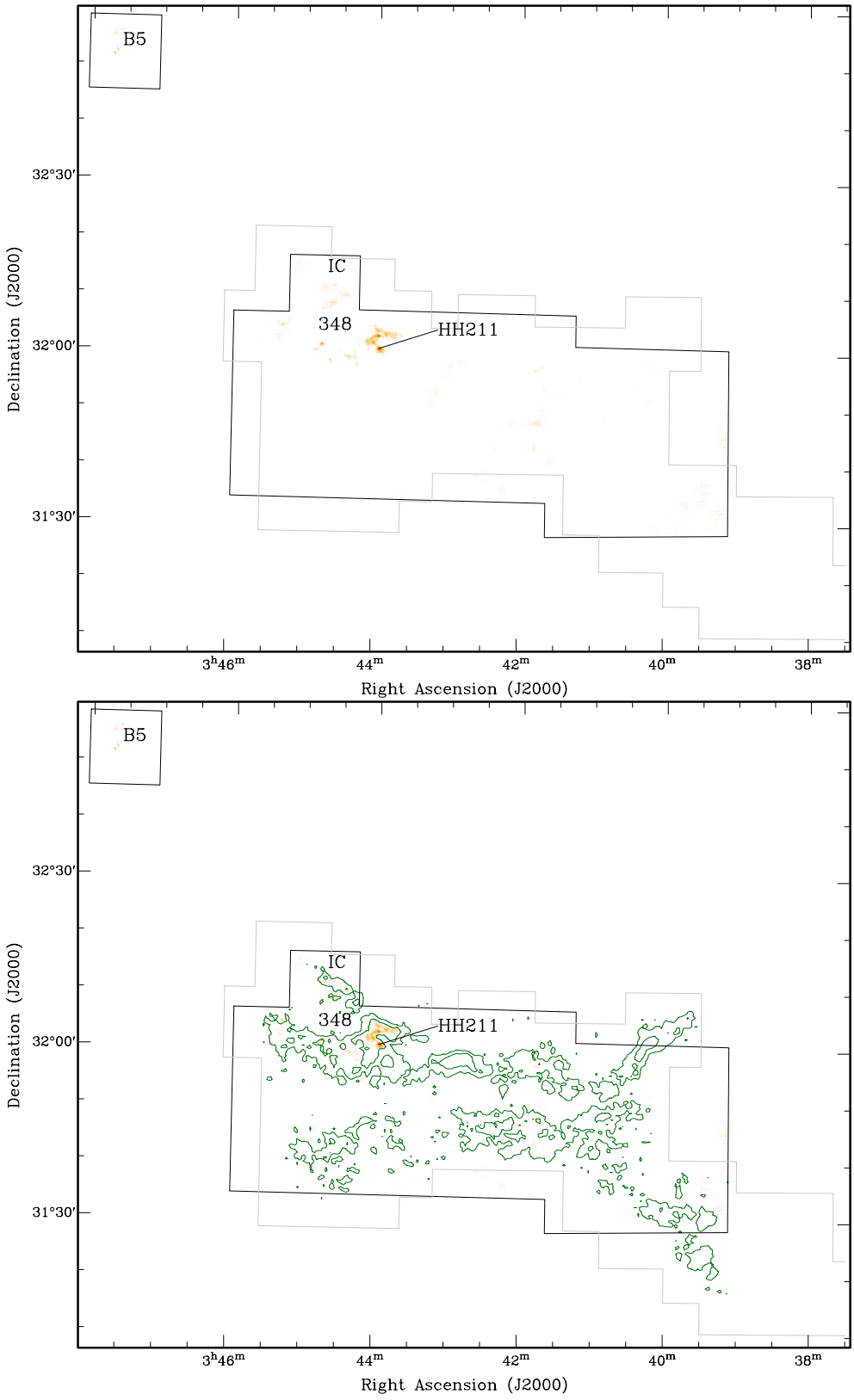

Fig. 1. a) The eastern part of the Perseus molecular cloud complex. *Top*: SCUBA 850 μm map. The colourscale (greyscale) is from 0 to 2281 mJy/beam on a square root (flux density) scale to bring out the low intensity features. *Bottom*: contours of $C^{18}O$ 1–0 integrated intensity at 1′ resolution overlaid on 850 μm colourscale (greyscale). Contours are 1, 2, 4, 8, 16 K km s^{-1}. In both maps the black boundary marks the area mapped with SCUBA and the grey boundary marks the area mapped in $C^{18}O$ (note, B5 was not mapped in $C^{18}O$). Some well-known clusters and IRAS sources are marked.

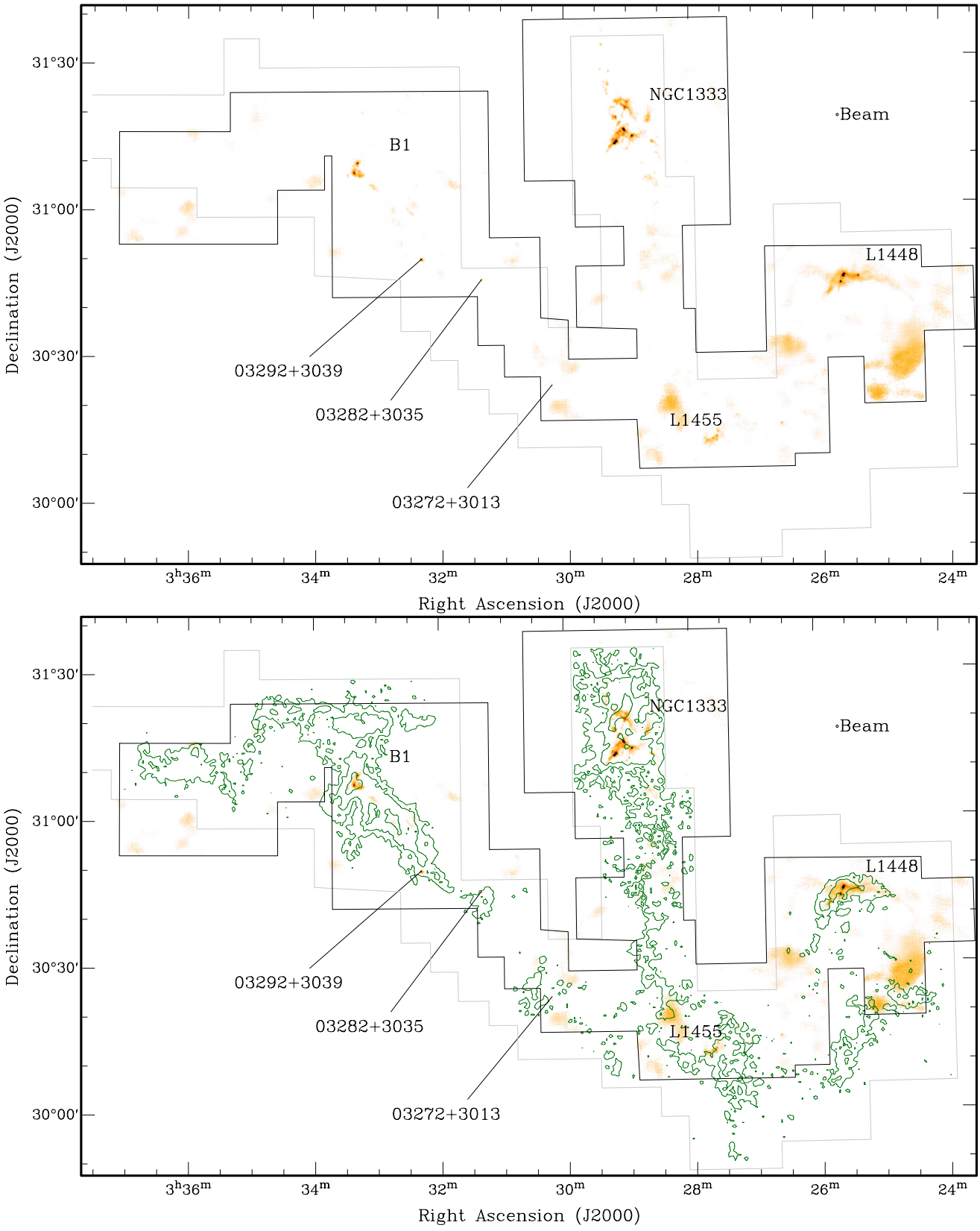

Fig. 1. b) The western part of the Perseus molecular cloud complex. *Top*: SCUBA 850 μm map. The colourscale (greyscale) is from 0 to 2281 mJy/beam on a square root (flux density) scale to bring out the low intensity features. *Bottom*: contours of $C^{18}O$ 1–0 integrated intensity at 1′ resolution overlaid on 850 μm colourscale (greyscale). Contours are 1, 2, 4, 8, 16 K km s^{-1}. In both maps the black boundary marks the area mapped with SCUBA and the grey boundary marks the area mapped in $C^{18}O$ (note, B5 was not mapped in $C^{18}O$). Some well-known clusters and IRAS sources are marked.

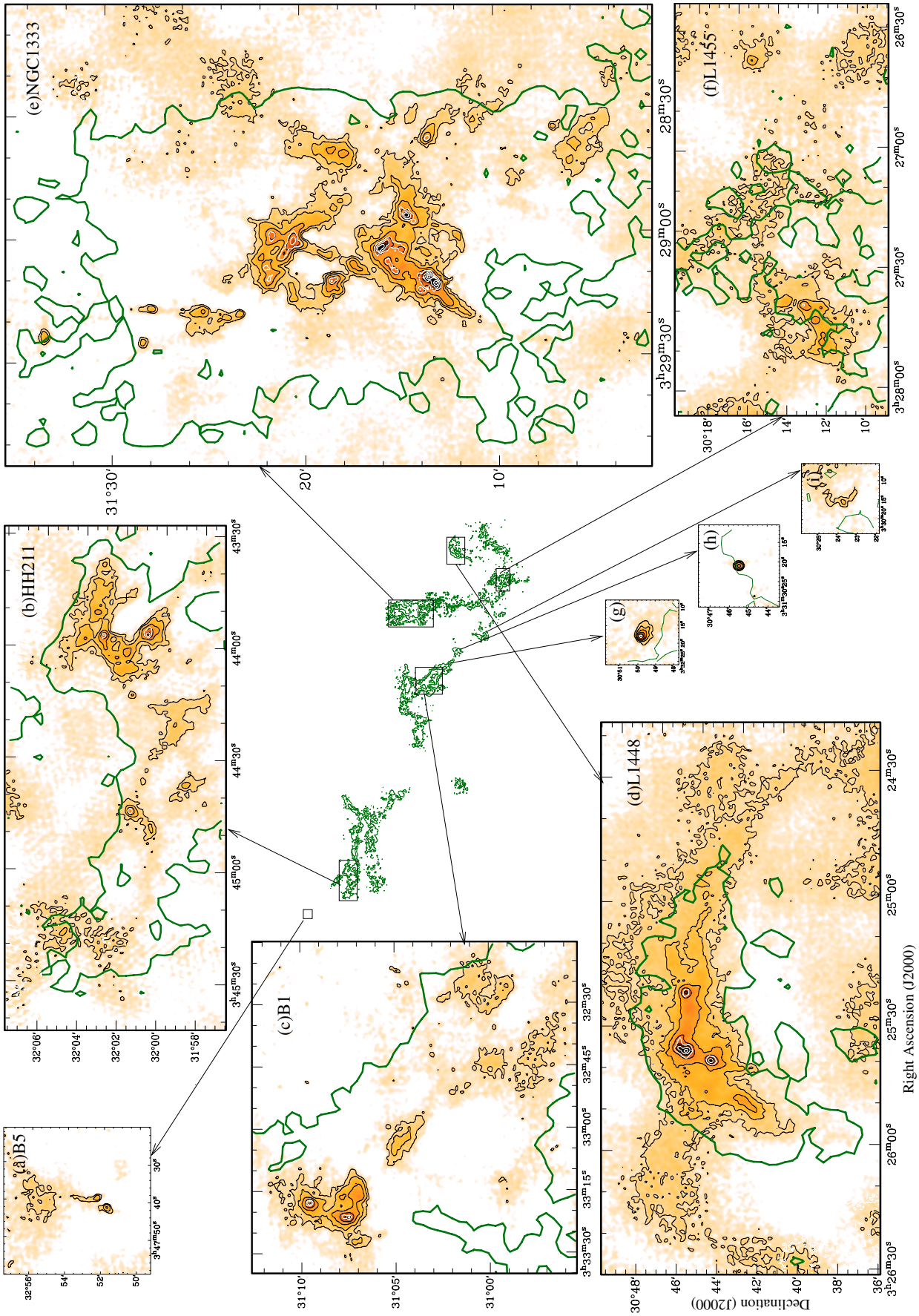

Fig. 2. SCUBA 850 μm maps of the **a)** B5, **b)** HH211, **c)** B1, **d)** L1448, **e)** NGC 1333, **f)** L1455, **g)** IRAS 03292+3039, **h)** IRAS 03282+3035 and **i)** IRAS 03271+3213 regions. Colourscale (greyscale) is 850 μm continuum from 0 (white) to 2281 mJy/beam (black) on a square root (flux density) scale to bring out the low intensity features. Black contours are 850 μm 100, 200, 400, 800, 1600, 3200 mJy/beam. White contours are 450 μm 2, 4, 8 Jy/beam. Dark green contours (thick grey contours) are where the $C^{18}O$ integrated intensity = 1 K km s^{-1}.

more detail in Fig. 2, where the individual cores and the filamentary structure connecting them are more evident. A full inventory of the pre/protostellar population of Perseus including estimates of individual core masses will form the basis of a later publication, but it is clear from the submm fluxes that these groups contain up to a few solar masses of stars.

Lower flux sources appear slightly less clustered than stronger sources (78% of sources with $F_{850\,\mu\mathrm{m}} < 250$ mJy are in clusters compared to 88% of sources with $F_{850\,\mu\mathrm{m}} > 500$ mJy), but this may be due to our core selection technique, which is less sensitive to weak cores in clusters (see Sect. 2). While there may be additional physical reasons why higher mass (and therefore brighter submm) sources preferentially form in clusters, we are not yet in a position to test this.

Making a count of cores, we find that more than 80% of the cores fall into five main clusters. We define a core to be in a cluster if it has 2 or more neighbours within 0.5 pc. With our sensitivity to all cores above 0.4 $M_\odot$, this definition guarantees a mass surface density of these regions of at least 1.2 $M_\odot$ within 1 pc^2. This definition is then consistent with the Spitzer tidal stability criterion that a stellar density $>1.0\ M_\odot\ \mathrm{pc}^{-3}$ is required in order for a cluster not to be disrupted on a timescale $\sim 10^8$ yr (Spitzer 1958), although during star formation clusters almost certainly rely on the gravitational potential of the molecular gas for binding. The remaining few isolated cores are scattered throughout the molecular cloud. 80% is probably a lower limit on the fraction of star formation in clusters in Perseus because we underestimate the number of cores in clusters due to confusion (see below). Infrared studies of embedded clusters of pre-main-sequence stars estimate the fraction of stars in clusters as 60–90% (L1630; Lada et al. 1991) and 50–100% (4 nearby clouds; Carpenter 2000), which are consistent with our findings.

This clustered mode of star formation contrasts with the Taurus region (Andre & Montmerle 1994), where isolated star formation dominates. With the majority of stars in the Galaxy forming in clusters (Lada & Lada 2003), Perseus, like Orion B (Mitchell et al. 2001) is more likely representative of typical star formation in our Galaxy.

3.1. Core clusters and stellar clusters

Two of the groups of cores are spatially associated with young stellar clusters: the HH211 group can be associated with IC 348, and the NGC 1333 cores with the NGC 1333 cluster, and may be evidence for continuing star formation in these clusters. We now consider the evolution of star formation in these regions by comparing the number of stars in the clusters with the likely stellar yield of the current protostellar cores.

As our pre/protostellar core sample is incomplete below 0.4 $M_\odot$, we take this as the lower mass limit for the count. The yield (in stars above 0.4 $M_\odot$) of the protostellar cores can only be a rough estimate because of the unknown multiple star fraction and the unknown final masses of the accreting stars. We assume each core yields between 1 and 2 stars above 0.4 $M_\odot$; this takes into account complex cores forming multiple stars.

In IC 348, the infrared population is consistent with continuous star formation at a rate of 50 stars with masses above 0.4 $M_\odot$ per Myr from 3.5 Myr to 0.5 Myr ago (Muench et al. 2003, based on an estimate that 2/5 of the total of 348 stars shown on the IMF in their Fig. 16, have masses above 0.4 $M_\odot$), This value and a constant star formation rate, suggests ~25 embedded protostars would be expected, if the embedded phase has a lifetime of 0.5 Myr. This is consistent with the 18 submm cores, containing an estimated 18–35 protostars, we detect in the HH211 region.

Taking an age spread and population for NGC 1333 of 0.5–1.5 Myr and 143 pre-main-sequence stars (Wilking et al. 2004), a constant star formation rate would predict ~70 protostars in the last 0.5 Myr, whereas we observe 36 cores containing an estimated 36–70 protostars. Here the submm population appears consistent or a little less than that expected from a constant star formation rate and an embedded phase lifetime of 0.5 Myr.

An embedded phase lifetime of 0.5 Myr is consistent with the youngest T Tauri sources in IC 348 and NGC 1333, but is longer than estimates for the embedded phase lifetime in ρ Ophiuchus and Taurus-Auriga, 0.1–0.4 Myr (Wilking et al. 1989; Kenyon et al. 1990). The age spread of T Tauri populations is notoriously difficult to estimate from isochrones (Hartmann 2001), and the youngest IC 348 and NGC 1333 infrared members may well be less than 0.5 Myr old. However, an embedded phase lifetime as short as 0.1 Myr would require either a significant correction to the T Tauri ages or that we happen to be looking at a star formation burst after a significant gap in both IC 348 and NGC 1333, which seems unlikely.

In conclusion, in IC 348 and NGC 1333 our observations are consistent with a steady or reduced star formation rate over the last 0.5 Myr, but not an increasing one.

The small population of cores in many of the clusters in Perseus raises the question of the cluster IMF – how many stars form in large/massive clusters compared to small ones? The massive NGC 1333 cluster, which has a stellar population of 143 stars with a total stellar mass of 79 $M_\odot$ (Lada et al. 1996) contains 40% of our pre/protostellar cores. A further 15% lie in the HH211 region bordering IC 348, which has >300 stellar members, and 160 $M_\odot$ (Luhman et al. 2003). So, in Perseus, 40–60% of cores are in massive clusters having >50 $M_\odot$. On the other hand small clusters and isolated objects also contribute 40–60%, much more than the 10% suggested from the infrared studies: Lada & Lada (2003) suggest that 20–50 $M_\odot$ clusters contribute no more than 10% of all stars. Unlike our statistics on cores, our statistics on clusters are derived from a very small sample of 5, so are less certain. Nevertheless, although the infrared and submillimetre observations are sensitive to similar ranges of masses of stars (>0.1–0.3$M_\odot$; Carpenter 2000), the difference in age between the submillimetre sources and the infrared visible stars may explain this discrepancy. It is quite likely that the small protostellar clusters are not stable and therefore do not classify as clusters by the Lada & Lada criteria (>35 members obeying the Spitzer tidal stability criterion) by the time they have become visible at near infrared wavelengths. At a typical velocity of 1 km s^{-1} a star moves 1 pc in 1 Myr

or 10′ at the distance of Perseus. A small group of <10 prestellar cores which evolved to form a 1 Myr pre-main-sequence population scattered over a volume 20′ in diameter could well remain unidentified as a cluster in the infrared. Therefore infrared estimates of the amount of star formation in small groups may be biassed low. On the other hand, in the submm, by taking a snapshot at the earliest stages of star formation, we underestimate the count of objects in clusters because future star formation is not counted. The smaller clusters may yet go on to form many more stars. Specifically, B1 has a large reservoir of molecular gas and no known population later than Class I, and so may be at the earliest stages of cluster formation.

The total mass of gas above a column density threshold of 6×10^{22} cm^{-2} in the clusters and cores is estimated from the dust emission to be ∼2600 $M_\odot$. This assumes isothermal 12 K dust: the mass will be lower if the temperature is higher, as is the case around the protostars. Lowering the flux threshold from the 5σ level to include more low column density material would result in a higher mass. A 5σ cutoff is used to avoid contributions from artefacts on large spatial scales due to the reconstruction of the chopped map. With the 5σ cutoff, this contribution is limited to be less than 30% of the total: the mass estimate for the clusters alone (NGC 1333, HH211, B1, L1448, L1455) is 1800 $M_\odot$. The mass fraction of the molecular cloud actively involved in star formation at this time is less than 20% of the total gas mass of 17 000 $M_\odot$ estimated from the visual extinction (Bachiller & Cernicharo 1986b). The mass of dense molecular gas traced by C^{18}O 1–0, which has a column density threshold for detection of 1.6×10^{21} cm^{-2} ($A_\mathrm{v} \simeq 2$) and a critical density of 400 cm^{-3}, is ∼6000 $M_\odot$, lower than the mass estimate from extinction as it excludes low density and atomic gas. Thus a greater fraction of high column density gas than low column density gas is in the active star formation regions, up to as much as half of the gas above $A_\mathrm{v} \simeq 2$.

4. Filaments

The SCUBA 850 μm image shows filamentary structure throughout the cloud (Fig. 2). The active protostellar clusters are linked to dense filaments: the horseshoes of HH211 and B1, the arcs of L1455 and L1448, and the zigzag of dense gas in NGC 1333. Weaker filaments imaged by SCUBA to the east of HH211, the south of B1, the south of NGC 1333 and around L1448 each reach up to 1 pc in length, with the upper limit here presumably set by our sensitivity limit. The dust filaments have typical full width half maxima of 1′. Filaments to the east of the HH211 cluster and to the southwest of B1 do not appear to be connected to current protostellar activity but may be fragmenting into cores to form the next round of stars. All the filaments show intensity fluctuations along their length, with the most fragmented filaments already identified as strings of cores.

On much larger scales, ∼20 pc, the C^{18}O map (Fig. 1), which traces material down to lower column densities, also shows filamentary structure. The dust filaments detected by SCUBA are found in regions of high C^{18}O column density. In fact the entire Perseus cloud can be described as consisting of one filament with a continuous velocity structure along the cloud (Bachiller & Cernicharo 1986a). SCUBA detects 850 μm emission at the 5-σ level at H_2 column densities of $\sim 6 \times 10^{22}$ cm^{-2} ($A_\mathrm{v} \simeq 60$), as the C^{18}O starts to become optically thick. This column density is rarely reached and the SCUBA map is mostly empty. Some extended structure is also lost in the reconstruction of the SCUBA maps because of the limited range of chop throws.

The filaments are strongly reminiscent of structures formed in turbulent flows (Mac Low & Klessen 2004). What we see in the dust continuum is that the filaments are observed down to the small scales and high densities associated with cluster formation. This suggests that not only do molecular clouds on the parsec scales of the whole Perseus molecular cloud form by turbulence, but that the role of the filaments persists down to the cluster formation scale. A more detailed investigation of the role of turbulence, including kinematical information from molecular lines, is left to a future paper.

The mass in the filaments is substantial with a mean mass per unit length of between 4.7 and 11.5 $M_\odot$ per 0.1 pc (∼1′), assuming the filaments are isothermal at 12 K, and taking a sample of 43 filament cross-sections. The uncertainty is due to the subtraction of background flux, some of which is extended flux belonging the filaments and some of which is an artefact of the reconstruction process. An estimate of the artificial background in regions of blank sky suggests that the true filament mass lies roughly midway between these values.

The filament mass per unit length of 5–11 $M_\odot$ per 0.1 pc (1′) is 2–4 times the traditional thermal Jeans mass for a Jeans length of 0.1 pc but this does not imply that the filaments have to be unstable. The criteria for a filament are different for those of a uniform medium (Larson 1985). Theoretical models for filaments range from a simple non-magnetic isothermal filament (Ostriker 1964) to magnetised filaments with helical fields which can be toroidal or poloidal or both (Tilley & Pudritz 2003; Fiege & Pudritz 2000; Fiege et al. 2004). A key prediction from these models is the ratio of the mass per unit length m to the cylindrical virial mass per unit length m_vir, which is given by

$$m_\mathrm{vir} = \frac{2\langle\sigma_\mathrm{tot}^2\rangle}{G},$$

where σ_tot is the 1-dimensional total (thermal plus non-thermal) velocity dispersion of the average gas molecule. For filaments with or without magnetic field,

$$\frac{m}{m_\mathrm{vir}}\left(1 - \frac{M}{|W|}\right) = 1 - \frac{P_\mathrm{S}}{\langle P\rangle},$$

where $M/|W|$ is the ratio of magnetic energy to gravitational energy per unit length. Following Fiege & Pudritz (2000) Table 2, we assume the external pressure to be $10^{4.5}$ K cm^{-3}, and estimate the internal pressure from

$$P/k = \frac{\rho\sigma_\mathrm{tot}^2}{k} = 2 \times 10^6 \text{ K cm}^{-3}$$

using an average density in the filaments of 10^5 cm^{-3}. The exact values of these quantities are unimportant; what is important is that the ratio of external to internal pressure $P_\mathrm{S}/\langle P\rangle \simeq 0.01$,

which is much less than 1, so there are three regimes: $m/m_{\rm vir} \sim 1$, the filament can exist without magnetic support, $m/m_{\rm vir} \gg 1$ a supporting poloidal field is required, and $m/m_{\rm vir} \ll 1$, when a binding toroidal field is required (see Fiege & Pudritz 2000; Fiege et al. 2004, for details).

From a sample of 7 $C^{18}O$ 1–0 spectra towards filaments, we measure velocity *FWHM* of 0.6–1.0 km s^{-1}. The conversion from velocity *FWHM* $\Delta v_{\rm obs}$ measured in $C^{18}O$ to $\sigma_{\rm tot}$, taking into account that the $C^{18}O$ molecule is more massive than the predominant H_2, is

$$\sigma^2_{\rm tot} = \frac{1}{8\ln 2}\left(\Delta v^2_{\rm obs} + 8\ln 2 \frac{kT}{m_{\rm P}}\left(\frac{1}{\bar{m}} - \frac{1}{m_{\rm C18O}}\right)\right),$$

where $m_{\rm P}$ is the proton mass, $\bar{m} = 2.33$ assuming 1 He for every 5 H_2 molecules, $T = 10$ K, and $m_{\rm C18O} = 30$.

The measured $C^{18}O$ linewidths correspond to virial masses of 45–100 $M_\odot$ pc^{-1}, compared to the measured mass per unit length of 47–115 $M_\odot$ pc^{-1}. This simple analysis suggests that the Perseus star forming filaments are consistent with being non-magnetic filaments (Ostriker 1964).

This last result disagrees with the Fiege & Pudritz (2000) studies of star-forming filaments, which typically used ^{13}CO linewidths, and found $m/m_{\rm vir} < 1$. From a sample of 8 ^{13}CO 1–0 spectra, we measure velocity *FWHM* of 1.4–2.0 km s^{-1}, typically a factor of 2 greater than $C^{18}O$ linewidths. If instead these ^{13}CO linewidths are representative of the velocity field within the filaments then ours too require additional binding by a toroidal field. However, it seems more likely to us that the $C^{18}O$ linewidths are more appropriate for the thermal support within the dense filaments, as $C^{18}O$ profiles are less affected by optical depth, and that the correct solution is one where the total toroidal field is small.

The mass derived from the dust emission, which increases if either the dust temperature or the 850 μm emissivity is lower than those assumed, both of which are possibilities, adds another uncertainty. An examination of the transverse column density structure and the dust polarisation would provide a further test of the filament support but this is beyond the scope of the current paper.

The alternative conclusion that could be reached from the high virial mass is that the filaments are not stable but transient, dispersing on the crossing time of 0.1 Myr (assuming a filament width of 0.1 pc and velocity dispersion from $C^{18}O$ of $\sigma_{\rm tot} = 0.4$ km s^{-1}). If this is true, then the star formation which is clearly occurring in the filaments must also happen on a crossing time.

Given filament masses of 5–11 $M_\odot$ per 0.1 pc, there is no requirement for substantial large scale flows along or onto the filaments in order to gather sufficient material for further star formation. Typically, in regions where cores have already formed, one or two cores are found within 0.1 pc, and local fragmentation will suffice to explain their masses. On the other hand, each filament does not hold a vast reservoir of mass – a few tens of $M_\odot$. Therefore the filaments are not required to disperse large fractions of their mass in order to remain consistent with the observed stellar densities in IC 348 or NGC 1333. In other words the conversion of dense molecular gas into stars may be fairly efficient once the filament stage is reached, and most of the filament mass may ultimately go into cores. This potentially high conversion efficiency of dense molecular gas into stars has also been noticed for NH_3 cores (Fuller & Myers 1987). Alternatively, stellar clusters may be built up by a series of filaments that form a few stars inefficiently, disperse, and are replaced, requiring ongoing filament production in the same location.

5. Column density condition for star formation

We are interested in the conditions under which stars form and it is clear that the density of the parent molecular cloud is an important factor. Density itself is not so easy to measure directly from dust continuum or $C^{18}O$ emission, but what we can consider is how the numbers of stars formed varies with the line-of-sight column density (or equivalently visual extinction). An extinction threshold for star formation at $A_{\rm v} = 7$–9 was found in both Taurus and Ophiuchus (Johnstone et al. 2004; Onishi et al. 1998), which could indicate that a certain amount of shielding from the interstellar radiation field is required for star formation to occur. Onishi et al. (1998) measured the column density of $C^{18}O$ associated with sources in Taurus, and found that the cold IRAS sources (assumed to be the younger protostars) and starless $H^{13}CO^+$ cores had a average column density of at least 8×10^{21} cm^{-2} or $A_{\rm v} = 9$. Johnstone et al. (2004) compared 850 μm cores in ρ Ophiuchus with an optical/IR extinction map and found no submm cores below an $A_{\rm v}$ of 7. In both cases the interpretation is that star formation is inhibited below a certain $A_{\rm v}$.

The $C^{18}O$ integrated intensity is a good tracer of total gas column density over the typical range of column densities in molecular clouds, but is less reliable at extreme column densities. At low column densities the $C^{18}O$ abundance falls due to photodissociation. On the other hand at high densities the line becomes optically thick and in addition in low temperature, high density regions the $C^{18}O$ depletes onto dust grains (e.g. Tafalla et al. 2004) and so ceases to trace the gas. But between these extremes, a linear $C^{18}O$ – $A_{\rm v}$ relationship holds above $A_{\rm v} \sim 4$ (Frerking et al. 1982).

We see in Fig. 1 that the $C^{18}O$ is relatively smooth on scales of a few arcminutes across the cloud, rather than peaking at the submm cores. $C^{18}O$ integrated intensity at 1′ resolution is a poor tracer of submm cores, tracing instead the environment on larger scales. This is probably largely due to beam dilution – the $C^{18}O$ effective beam area is $(1'/14'')^2 = 18$ times greater than the 850 μm beam, so a core of as much as 0.7 $M_\odot$ could produce less than 1 K km s^{-1} in $C^{18}O$ integrated intensity if it had no extended envelope. Depletion also helps reduce the contribution of core emission to the $C^{18}O$. $C^{18}O$ depletion has been measured in prestellar cores on scales of 0.1 pc (Tafalla et al. 2004), with the $C^{18}O$ abundance substantially reduced in the dense parts of the cores. Finally, the $C^{18}O$ 1–0 line saturates at about the same column density at which the SCUBA 850 μm emission becomes visible, which further reduces the contribution from the highest column density lines-of-sight. The result is that the $C^{18}O$ traces the environment of the cores, and thus, if we look at young enough cores, the environment in which cores form.

Table 1. Fraction of cloud by area and number of cores in each $C^{18}O$ integrated intensity range.

$I(C^{18}O)$ K km s^{-1}	A_v	% area[1]	N(cores)	% of cores
<1	<5.2	83	10	11.4
1–2	5.2–8.8	13	14	15.9
2–3	8.8–12.4	3	32	36.4
3–4	12.4–15.9	0.5	17	19.3
4–5	15.9–19.5	0.2	13	15.9
>5	>19.5	0.04	1	1.1

[1] Fraction of the area of the cloud mapped in $C^{18}O$.

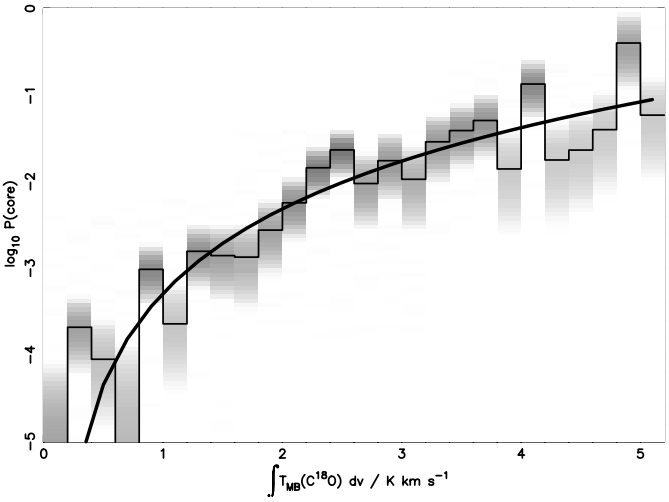

Fig. 3. Probability of finding a submm core in a 22″ square pixel with a given 1′ beam-averaged $C^{18}O$ integrated intensity: observed (thin black line) and probability distribution of $\log_{10}(P(\mathrm{core})) = N_{\mathrm{cores}}(I_i)/N_{\mathrm{pixels}}(I_i)$ for each integrated intensity bin I_i (greyscale), and best-fit power law (thick black line). To convert the probabilities to another pixel size use $P' = P(\mathrm{core}) \times \frac{(\mathrm{pixel\ area})}{22^2}$.

5.1. Probability of finding a core

In this section we investigate how the probability of finding a core varies with the $C^{18}O$ integrated line intensity on arcminute scales.

Table 1 compares the area of the cloud in each $C^{18}O$ integrated intensity range with the number of submm cores in that region. Although there are clearly cores associated with areas of the cloud with a wide range of cloud column densities, cores are much more likely to be found in regions of high column density. In Fig. 3 we demonstrate this graphically by plotting the probability of finding a submm core, P(core), as a function of integrated $C^{18}O$ intensity, $I(C^{18}O)$ (K km s^{-1}). The probability of finding a core is derived from two observed distributions. The first is the $C^{18}O$ integrated intensity towards the peak of each submm core, determined from the $C^{18}O$ map (Fig. 1b). We bin the results by $C^{18}O$ integrated intensity to generate $N_{\mathrm{cores}}(I_i)$, the number of submm cores in each integrated intensity bin. The second is a count of the number of pixels in the map in each integrated intensity bin, $N_{\mathrm{pixels}}(I_i)$. This gives a measure of the (probability) distribution of integrated intensities $P(I)$ in the surveyed cloud, or in other words how much of the cloud area lies in a particular integrated intensity range. The probability of finding a submm core at a position with $C^{18}O$ integrated intensity I is then given by $P(\mathrm{core}) = N_{\mathrm{cores}}(I)/N_{\mathrm{pixels}}(I)$.

As both distributions $N_{\mathrm{cores}}(I_i)$ and $N_{\mathrm{pixels}}(I_i)$ at some point contain very small numbers of counts we have to be very careful with the error budget in calculating this quotient. We take the Bayesian approach detailed in Appendix A to calculate P(core).

Figure 3 shows that P(core) is a steeply increasing function of integrated intensity I. In other words, the probability of finding a core increases rapidly with $C^{18}O$ column density. Fitting (for simplicity, and for want of a theoretical prediction) a power law kI^{α} to the distribution gives a best fit result of $\alpha = 3.00^{+0.18}_{-0.21}$, $\log_{10} k = -3.15 \pm 0.08$ (uncertainties are 68.3% confidence limits). k is the scaling factor which gives the probability of finding a core in a 22″ square pixel. A power law must break down as a description of P(core) at high $I(C^{18}O)$ as the probability of finding a core in any one pixel approaches 1 but this limit is not approached with our pixel size.

The exact shape of the distribution is uncertain at the low end because of incomplete map coverage and lack of sensitivity. Both JCMT and FCRAO maps have limited coverage of low column density regions, and as the area mapped in $C^{18}O$ is larger, we may have missed SCUBA cores. So we may underestimate (by only a few cores, we believe) the probability of finding a core below $I(C^{18}O) = 1.0$ K km s^{-1}. Figure 1 also shows that the $C^{18}O$ observations were not biassed towards regions with SCUBA clumps, so we do not overestimate the number of cores at low intensity. The measurement uncertainties also become significant below $I(C^{18}O) = 1$ K km s^{-1} ($A_v = 5.2$) – the $C^{18}O$ rms is 0.3 K km s^{-1}. Therefore, the source count in the lower 5 integrated intensity bins (Fig. 3) is also uncertain. We made a fit excluding the lowest column density channels ($I(C^{18}O) < 1.0$ K km s^{-1}), which steepens the power law to $\alpha = 3.45 \pm 0.27$, a change which is significant only at the 95% level.

What does $P(\mathrm{core}) \propto I^{3.0}$ mean? We can rule out an absolute threshold in $N(C^{18}O)$ (and by implication A_v) for submm cores (though not necessarily for star formation). There are clearly real submm cores at low $C^{18}O$ integrated intensities of 4 K km s^{-1} or visual extinctions as low as $A_v = 3$ ($N(H_2) = 2.7 \times 10^{21}$ cm^{-2}). At these column densities the uncertainty on the $C^{18}O$ data is high but the low extinctions are independently confirmed by ^{13}CO data from the same observing run. There are submm cores at very low $C^{18}O$ column density despite the fact that the peak column densities in the cores must be high to be detected with SCUBA, and that the observations are less sensitive to the larger, more diffuse cores which form in low pressure regions (Sect. 2).

The 10% of cores with $I < 1.0$ K km s^{-1} include the L1455 cluster plus IRAS 03235+3004, 03422+3256, and 03262+3123. The question remains whether stars can form

at these low column densities or if these low column density cores are all more evolved (Class I) protostars, or whether the lower angular resolution of the line data is biasing the column density estimate to a low value. Certainly the majority of the $I < 1$ K km s^{-1} ($A_v < 5.2$) sources have IRAS identifications and are therefore likely to be classified as Class I. Potentially less evolved cores are L1455 smm1 ($\alpha(2000) = 03^h27^m42\overset{s}{.}9$, $\delta(2000) = +30°12'28''$), which has a CO outflow, is definitely protostellar, and has low IRAS fluxes, L1455 smm2 ($\alpha(2000) = 03^h27^m46\overset{s}{.}6$, $\delta(2000) = +30°12'05''$; probably starless), and three weak cores to the west of B1 which may be noise artefacts. Onishi et al. (1998) found that cold cores in Taurus were only found at a high C^{18}O threshold of 8×10^{21} cm^{-2}, equivalent to I(C^{18}O) ~ 2.0 K km s^{-1} or $A_v = 9$, whereas warm cores (more evolved IRAS sources) could appear at lower C^{18}O column density. This appears to roughly hold in Perseus as well as Taurus, but we need to investigate this further once we can better classify the Perseus sources. All the submm cores in Ophiuchus lie at $A_v \geq 7$ (Johnstone et al. 2004). As the cores in Ophiuchus were identified in the same way as in this study of Perseus, that is, from SCUBA 850 μm observations, there must either be a real difference between star formation in the two clouds, or a significant difference in the way that optical/IR extinction and C^{18}O trace column density in the range $A_v = 2$–7. ρ Oph is lacking in starless cores and Class 0 protostars compared to other dark clouds and there may have been a burst of star formation 10^5 years ago in this region that has now tailed off (Visser et al. 2002); in Perseus, however, we have clear evidence for continuing star formation, so there are differences between the ages of the populations in the two clouds which might underly the differing column density thresholds, though the mechanism is unclear.

The $I^{3.0}$ power law rules out simple models in which the number of cores is proportional to the mass along the line-of-sight (P(core) $\propto I$). If density is the determining quantity for star formation, central densities must rise steeply with increasing column density. Theoretical models which reproduce the observed C^{18}O integrated intensity – core probability relationship are required to find the actual physics behind the $I^{3.0}$ power law (if indeed a power law is the right functional form).

This steep rise in P(core) with column density is consistent with the overall trend seen in star forming regions for high column density regions to be associated with formation of larger numbers of stars. Isolated low mass star formation in Taurus occurs at column densities of $\simeq 8$–15×10^{21} cm^{-2} (Onishi et al. 1998). Column densities for clustered star formation in Perseus reach 2×10^{22} cm^{-2}. In contrast, column densities in massive star forming regions typically exceed 10^{23} cm^{-2} (Hatchell et al. 1998).

We have already mentioned C^{18}O depletion and optical depth, both of which act to reduce the observed I(C^{18}O) for a given H_2 column density. If plotted against H_2 column density, the P(core) distribution would flatten at high column densities. A rough correction for the optical depth suggests that the power law index could reduce from 3.0 to ~2.0 in the worst case. This is still significantly steeper than linear.

Given a C^{18}O map and the above P(core) vs. I(C^{18}O) relationship, we can now predict – at least statistically – how many submm cores will be found and how they will be distributed. It will be interesting to see how well this relationship holds in regions other than Perseus. There are obviously more factors involved in core formation than C^{18}O column density, and a better model of where stars form will need to take into account filaments, clustering and other factors.

6. Conclusions

We have mapped the submm dust emission from the Perseus molecular cloud with SCUBA at JCMT with 5000 AU resolution, revealing 91 embedded starless and protostellar cores and the filamentary structures which lead to star formation. The total mass of the Perseus cloud derived from extinction measurements is 17 000 $M_\odot$ (Bachiller & Cernicharo 1986b). Of this, 6000 $M_\odot$ is traced by C^{18}O and 2600 $M_\odot$ by dust in cores and clusters. We conclude:

1. Only a small fraction, less than 20%, of the mass of the molecular cloud is involved in star formation at this time.
2. By number, 80% of the star formation is occuring in clusters, defined by a stellar density of more than 1 $M_\odot$ pc^{-3}. Some current star formation activity may be associated with the larger stellar clusters IC 348 and NGC 1333, but about half the star formation is taking place in small clusters containing less than 35 members.
3. Filamentary structure is evident both in the molecular gas on 20 pc scales and on small scales in the dust emission. High column density dust filaments with masses per unit length of 5–11 $M_\odot$ per 0.1 pc are associated with the existing clusters. This range of masses is in agreement with models of filaments with either unmagnetised filaments or a slightly dominant toroidal field (Fiege & Pudritz 2000).
4. The probability of finding a submm core is a steeply rising function of column density (as measured by C^{18}O integrated intensity): P(core) $\propto I^{3.0}$. There is no C^{18}O column density cutoff (and by implication A_v) below which there are no cores.

These results are specific to Perseus, and it will require similar studies of a much larger sample of such clouds before we can fully understand which of these features are typical of star forming clouds and which are, for some reason, unique to Perseus.

Acknowledgements. We would like to thank Jane Buckle, Tak Fujiyoshi and others who spent long nights at the telescope collecting data as part of this project, and the referee Doug Johnstone for his careful reading and constructive suggestions. The James Clerk Maxwell Telescope is operated by the Joint Astronomy Centre on behalf of the Particle Physics and Astronomy Research Council of the UK, the Netherlands Organisation for Scientific Research, and the National Research Council of Canada. The FCRAO is supported by the NSF via AST-0100793. JH acknowledges support from DFG SFB 494 and the PPARC Advanced Fellowship programme. The National Radio Astronomy Observatory is a facility of the National Science Foundation operated under cooperative agreement by Associated Universities, Inc.

References

Andre, P., & Montmerle, T. 1994, ApJ, 420, 837
Bachiller, R., Andre, P., & Cabrit, S. 1991, A&A, 241, L43
Bachiller, R., & Cernicharo, J. 1986a, A&A, 168, 262
Bachiller, R., & Cernicharo, J. 1986b, A&A, 166, 283
Bachiller, R., Terebey, S., Jarrett, T., et al. 1994, ApJ, 437, 296
Barsony, M., Ward-Thompson, D., André, P., & O'Linger, J. 1998, ApJ, 509, 733
Bohlin, R. C., Savage, B. D., & Drake, J. F. 1978, ApJ, 224, 132
Carpenter, J. M. 2000, AJ, 120, 3139
Chandler, C. J., & Richer, J. S. 2000, ApJ, 530, 851
Chini, R., Reipurth, B., Sievers, A., et al. 1997, A&A, 325, 542
Chini, R., Ward-Thompson, D., Kirk, J. M., et al. 2001, A&A, 369, 155
Churchwell, E., Wolfire, M. G., & Wood, D. O. S. 1990, ApJ, 354, 247
de Zeeuw, P. T., Hoogerwerf, R., de Bruijne, J. H. J., Brown, A. G. A., & Blaauw, A. 1999, AJ, 117, 354
Dent, W. R. F., Matthews, H. E., & Ward-Thompson, D. 1998, MNRAS, 301, 1049
Draine, B. T., & Lee, H. M. 1984, ApJ, 285, 89
Eislöffel, J., Froebrich, D., Stanke, T., & McCaughrean, M. J. 2003, ApJ, 595, 259
Fiege, J. D., Johnstone, D., Redman, R. O., & Feldman, P. A. 2004, ApJ, 616, 925
Fiege, J. D., & Pudritz, R. E. 2000, MNRAS, 311, 85
Frerking, M. A., Langer, W. D., & Wilson, R. W. 1982, ApJ, 262, 590
Fuller, G. A., & Myers, P. C. 1987, in Physical Processes in Interstellar Clouds, NATO ASIC Proc., 210, 137
Gooch, R. 1996, in Astronomical Data Analysis Software and Systems V, ASP Conf. Ser., 101, 80
Hartmann, L. 2001, AJ, 121, 1030
Hatchell, J., Thompson, M. A., Millar, T. J., & MacDonald, G. H. 1998, A&AS, 133, 29
Hirano, N., Kamazaki, T., Mikami, H., Ohashi, N., & Umemoto, T. 1999, in Star Formation 1999, Proceedings of Star Formation 1999, held in Nagoya, Japan, June 21–25, 1999, ed. T. Nakamoto, Nobeyama Radio Observatory, 181
Jenness, T., & Lightfoot, J. F. 1998, in Astronomical Data Analysis Software and Systems VII, ASP Conf. Ser., 145, 216
Jennings, R. E., Cameron, D. H. M., Cudlip, W., & Hirst, C. J. 1987, MNRAS, 226, 461
Johnstone, D., Di Francesco, J., & Kirk, H. 2004, ApJ, 611, L45
Kenyon, S. J., Hartmann, L. W., Strom, K. M., & Strom, S. E. 1990, AJ, 99, 869
Lada, C. J., Alves, J., & Lada, E. A. 1996, AJ, 111, 1964
Lada, C. J., & Lada, E. A. 2003, ARA&A, 41, 57
Lada, E. A., Evans, N. J., Depoy, D. L., & Gatley, I. 1991, ApJ, 371, 171
Larson, R. B. 1985, MNRAS, 214, 379
Looney, L. W., Mundy, L. G., & Welch, W. J. 2000, ApJ, 529, 477
Luhman, K. L., Stauffer, J. R., Muench, A. A., et al. 2003, ApJ, 593, 1093
Mac Low, M., & Klessen, R. S. 2004, Rev. Mod. Phys., 76, 125
Matthews, B. C., & Wilson, C. D. 2002, ApJ, 574, 822
McCaughrean, M. J., Rayner, J. T., & Zinnecker, H. 1994, ApJ, 436, L189
Meynet, G., & Maeder, A. 2000, A&A, 361, 101
Mitchell, G. F., Johnstone, D., Moriarty-Schieven, G., Fich, M., & Tothill, N. F. H. 2001, ApJ, 556, 215
Motte, F., & André, P. 2001, A&A, 365, 440
Muench, A. A., Lada, E. A., Lada, C. J., et al. 2003, AJ, 125, 2029
O'Linger, J., Wolf-Chase, G., Barsony, M., & Ward-Thompson, D. 1999, ApJ, 515, 696
Onishi, T., Mizuno, A., Kawamura, A., Ogawa, H., & Fukui, Y. 1998, ApJ, 502, 296
Ossenkopf, V., & Henning, T. 1994, A&A, 291, 943
Ostriker, J. 1964, ApJ, 140, 1056
Rengel, M., Froebrich, D., Hodapp, K., & Eislöffel, J. 2002, in The Origins of Stars and Planets: The VLT View, ed. J. Alves, & M. McCaughrean
Sandell, G., Aspin, C., Duncan, W. D., Russell, A. P. G., & Robson, E. I. 1991, ApJ, 376, L17
Sandell, G., & Knee, L. B. G. 2001, ApJ, 546, L49
Sandell, G., Knee, L. B. G., Aspin, C., Robson, I. E., & Russell, A. P. G. 1994, A&A, 285, L1
Shu, F. H., Adams, F. C., & Lizano, S. 1987, ARA&A, 25, 23
Sivia, D. S. 1996, Data Analysis: a Bayesian Tutorial (Oxford Science Publications)
Spitzer, L. J. 1958, ApJ, 127, 17
Steenbrugge, K. C., de Bruijne, J. H. J., Hoogerwerf, R., & de Zeeuw, P. T. 2003, A&A, 402, 587
Tafalla, M., Myers, P. C., Caselli, P., & Walmsley, C. M. 2004, A&A, 416, 191
Tilley, D. A., & Pudritz, R. E. 2003, ApJ, 593, 426
Visser, A. E., Richer, J. S., & Chandler, C. J. 2002, AJ, 124, 2756
Wilking, B. A., Lada, C. J., & Young, E. T. 1989, ApJ, 340, 823
Wilking, B. A., Meyer, M. R., Greene, T. P., Mikhail, A., & Carlson, G. 2004, AJ, 127, 1131

Online Material

Appendix A: Details of power law fitting procedure

In this Appendix we give details of the analysis of the core probability vs. $C^{18}O$ column density. We first assume that the counts in each integrated intensity bin I_i, $x_i = N_{\rm cores}(I_i)$ and $y_i = N_{\rm pixels}(I_i)$, obey Poisson statistics, i.e., are related to the true values μ_x and μ_y by:

$$P(x\,|\,\mu_x) = \frac{\mu_x^x \mathrm{e}^{-\mu_x}}{x!}, \qquad P(y\,|\,\mu_y) = \frac{\mu_y^y \mathrm{e}^{-\mu_y}}{y!}.$$

By Bayes' theorem we can reverse this. We take a a flat prior with a positivity constraint on μ_x and μ_y, $P(\mu_x) = 1\,(\mu_x \geq 0)$ or $0\,(\mu_x < 0)$ and similarly for μ_y (see, e.g., Sivia 1996 for an introduction to Bayesian data analysis). Then

$$P(\mu_x\,|\,x) = P(x\,|\,\mu_x) \times P(\mu_x) = \frac{\mu_x^x \mathrm{e}^{-\mu_x}}{x!} \tag{A.1}$$

$$P(\mu_y\,|\,y) = P(y\,|\,\mu_y) \times P(\mu_y) = \frac{\mu_y^y \mathrm{e}^{-\mu_y}}{y!} \tag{A.2}$$

and similarly for μ_y.

We calculate the data-derived probability of finding a core at integrated intensity I_i, $C_{{\rm obs},i} = x_i/y_i$ directly. However, this is only an estimate of the true value of C because of the uncertainties in x_i and y_i. We next calculate the PDF for the true value of finding a core $P(C_{\rm true}\,|\,x, y)$ given x_i and y_i. To obtain the probability distribution of the true quotient $C_{\rm true}$ given the observed x and y we rewrite the x distribution (Eq. (A.1)) in terms of μ_y and $C_{\rm true}$:

$$P(\mu_y\,|\,x, C_{\rm true}) = \frac{(C_{\rm true})^x \mathrm{e}^{-C_{\rm true}\mu_y}}{x!}. \tag{A.3}$$

Now with two probability distributions on μ_y (Eqs. (A.2) and (A.3)) we can multiply and integrate out μ_y:

$$\begin{aligned} P(C_{\rm true}\,|\,x, y) &\propto \int_0^\infty \frac{\mu_y^y \mathrm{e}^{-\mu_y}}{y!} \frac{(C_{\rm true})^x \mathrm{e}^{-C_{\rm true}\mu_y}}{x!} \mathrm{d}\mu_y \\ &\propto \frac{(x+y)^{(x+y)}}{(1+C_{\rm true})^{(x+y+1)}} \frac{C_{\rm true}^x}{x!y!}. \end{aligned}$$

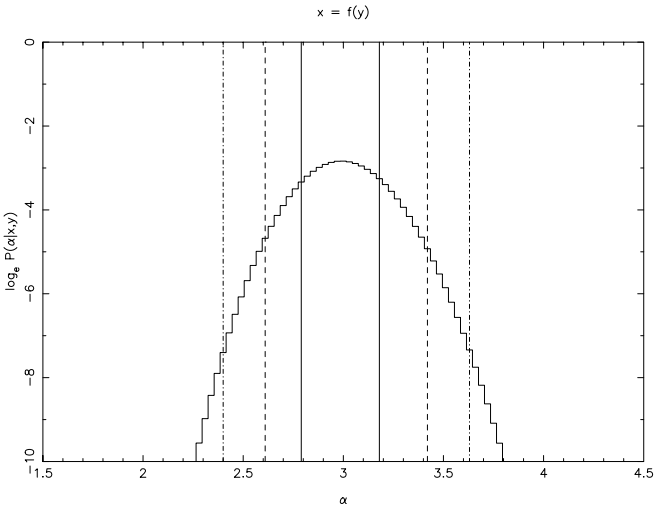

Fig. A.1. Probability density function for the power law index α, $\log(P(\alpha|x, y))$. Verticals are 68.3%, 95.4% and 99.7% confidence limits.

Finally to find the most probable power law fit, for each I_i we calculate $P(C_{\rm true}, i = kI_i^\alpha \mid x_i, y_i)$ from the previous formula and

$$P(k, \alpha \mid x, y) = \prod P(k, \alpha \mid x_i, y_i).$$

The PDFs for $C_{\rm true}$ are plotted as greyscales and contours for each integrated intensity bin in Fig. 3. We marginalise (integrate over) k and α in turn to estimate the uncertainties in each parameter individually as given in Sect. 5. The PDF for α is shown in Fig. A.1.

Table A.1. SCUBA 850 μm core positions, names and references, peak 850 μm fluxes and $C^{18}O$ integrated intensity at the submm peak position.

No.	RA_{2000} hh:mm:ss	Dec_{2000} dd:mm:ss	Cluster[1]	Name	Reference[2]	F_{850}[3] mJy/bm	$I(C^{18}O)$[4] K km s^{-1}
1	03:33:17.9	31:09:33	B1	B1-c	Matthews & Wilson (2002)	1638	4.0
2	03:33:21.4	31:07:31	B1	B1-bS	Hirano et al. (1999); Matthews & Wilson (2002)	1554	4.8
3	03:33:21.1	31:07:40	B1	B1-bN	Hirano et al. (1999); Matthews & Wilson (2002)	1200	4.8
4	03:33:16.3	31:06:54	B1	B1-d	Matthews & Wilson (2002)	514	4.1
5	03:33:01.9	31:04:23	B1	None		218	3.3
6	03:33:05.6	31:05:06	B1	None		207	2.8
7	03:33:16.5	31:07:51	B1	B1-a	Hirano et al. (1999); Matthews & Wilson (2002)	202	4.5
8	03:33:04.0	31:04:56	B1	None		202	2.9
9	03:33:03.0	31:04:38	B1	None		196	3.4
10	03:33:27.3	31:07:10	B1	None		179	4.2
11	03:33:00.3	31:04:17	B1	None		160	3.4
12	03:43:56.5	32:00:50	HH211	HH211	McCaughrean et al. (1994); Chandler & Richer (2000)	1494	2.5
13	03:43:56.9	32:03:05	HH211	IC 348 MMS	Eislöffel et al. (2003)	1032	3.1
14	03:44:43.9	32:01:32	HH211	None		623	2.0
15	03:43:50.8	32:03:24	HH211	No SMM/MM source		358	2.2
16	03:44:01.0	32:01:55	HH211	None		296	2.4
17	03:43:57.9	32:04:01	HH211	None		247	3.0
18	03:44:03.0	32:02:24	HH211	No SMM/MM source		237	2.5
19	03:44:36.8	31:58:49	HH211	None		234	1.8
20	03:44:05.5	32:01:57	HH211	No SMM/MM source		209	2.4
21	03:44:02.3	32:02:48	HH211	None		207	2.9
22	03:44:06.2	32:02:12	HH211	None		204	2.4
23	03:43:37.8	32:03:06	HH211	None		170	1.5
24	03:43:42.5	32:03:23	HH211	None		168	2.3
25	03:44:48.5	32:00:31	HH211	None		153	2.0
26	03:43:44.4	32:02:56	HH211	None		153	2.5
27	03:25:35.9	30:45:30	L1448	L1448NW	Looney et al. (2000); Barsony et al. (1998)	2300	2.9
28	03:25:36.4	30:45:15	L1448	L1448N B	Looney et al. (2000); Barsony et al. (1998)	2243	2.7
29	03:25:38.8	30:44:04	L1448	L1448 C	Bachiller et al. (1991); Barsony et al. (1998)	1737	2.3
30	03:25:22.4	30:45:11	L1448	L1448-IRS2	O'Linger et al. (1999)	1316	2.2
31	03:25:25.9	30:45:03	L1448	None		429	2.4
32	03:25:49.0	30:42:25	L1448	None		364	2.0
33	03:25:50.6	30:42:01	L1448	None		306	2.1
34	03:25:30.8	30:45:07	L1448	None		231	2.6
35	03:27:39.1	30:13:01	L1455	RNO 15 FIR	Rengel et al. (2002)	556	1.4
36	03:27:42.9	30:12:28	L1455	None		402	0.9

Table A.1. continued.

No.	RA_{2000} hh:mm:ss	Dec_{2000} dd:mm:ss	Cluster[1]	Name	Reference[2]	$F^{(3)}_{850}$ mJy/bm	$I(C^{18}O)^{(4)}$ K km s^{-1}
37	03:27:48.4	30:12:09	L1455	No SMM/MM source		324	0.8
38	03:27:46.6	30:12:05	L1455	No SMM/MM source		272	0.9
39	03:27:38.1	30:13:57	L1455	No SMM/MM source		238	1.4
40	03:27:39.9	30:12:10	L1455	None		232	1.4
41	03:29:10.4	31:13:30	NGC 1333	IRAS 4A	Sandell et al. (1991)	7000	3.7
42	03:29:12.0	31:13:10	NGC 1333	IRAS 4B; SK-3	Sandell et al. (1991); Sandell & Knee (2001)	3025	3.4
43	03:29:03.2	31:15:59	NGC 1333	HH7-11 MMS 1; SK-12/13	Chini et al. (1997)	2831	4.0
44	03:28:55.3	31:14:36	NGC 1333	IRAS 2A; SK-8	Sandell et al. (1994); Sandell & Knee (2001)	2355	3.8
45	03:29:01.4	31:20:29	NGC 1333	SK-24	Sandell & Knee (2001)	1119	3.7
46	03:29:10.9	31:18:27	NGC 1333	SK-20	Sandell & Knee (2001)	1061	3.6
47	03:28:59.7	31:21:34	NGC 1333	SK-31	Sandell & Knee (2001)	770	4.9
48	03:29:13.6	31:13:55	NGC 1333	IRAS 4C; SK-5	Looney et al. (2000); Sandell & Knee (2001)	667	3.3
49	03:28:36.7	31:13:30	NGC 1333	SK-6	Sandell & Knee (2001)	621	2.0
50	03:29:06.5	31:15:39	NGC 1333	HH 7-11 MMS 4; SK-15	Chini et al. (2001); Sandell & Knee (2001)	619	3.2
51	03:29:08.8	31:15:18	NGC 1333	SK-16	Sandell & Knee (2001)	574	2.8
52	03:29:03.7	31:14:53	NGC 1333	HH7-11 MMS 6; SK-14	Chini et al. (2001); Sandell & Knee (2001)	517	3.8
53	03:29:04.5	31:20:59	NGC 1333	SK-26	Sandell & Knee (2001)	513	4.8
54	03:29:10.7	31:21:45	NGC 1333	SK-28	Sandell & Knee (2001)	420	3.6
55	03:28:40.4	31:17:51	NGC 1333	None		410	1.9
56	03:29:07.7	31:21:57	NGC 1333	SK-29	Sandell & Knee (2001)	394	4.3
57	03:29:18.2	31:25:11	NGC 1333	SK-33	Sandell & Knee (2001)	376	4.1
58	03:29:24.0	31:33:21	NGC 1333	None		371	0.9
59	03:29:16.5	31:12:35	NGC 1333	None		371	3.2
60	03:28:39.3	31:18:27	NGC 1333	None		354	2.9
61	03:29:17.3	31:27:50	NGC 1333	None		349	2.3
62	03:29:07.1	31:17:24	NGC 1333	SK-18	Sandell & Knee (2001)	318	4.0
63	03:29:18.8	31:23:17	NGC 1333	SK-32	Sandell & Knee (2001)	308	3.8
64	03:29:25.5	31:28:18	NGC 1333	None		292	1.4
65	03:29:00.4	31:12:01	NGC 1333	SK-1	Sandell & Knee (2001)	288	2.3
66	03:29:05.3	31:22:11	NGC 1333	SK-30	Sandell & Knee (2001)	228	5.1
67	03:29:19.7	31:23:56	NGC 1333	None		223	4.7
68	03:28:56.2	31:19:13	NGC 1333	No SMM/MM source		201	3.9
69	03:28:34.4	31:06:59	NGC 1333	None		201	1.3
70	03:29:15.3	31:20:31	NGC 1333	SK-22	Sandell & Knee (2001)	192	4.2
71	03:28:38.7	31:05:57	NGC 1333	None		177	1.9
72	03:29:19.1	31:11:38	NGC 1333	No SMM/MM source		167	2.6
73	03:28:38.8	31:19:15	NGC 1333	None		162	2.4
74	03:28:32.5	31:11:08	NGC 1333	None		156	1.9

Table A.1. continued.

No.	RA_{2000} hh:mm:ss	Dec_{2000} dd:mm:ss	Cluster[1]	Name	Reference[2]	$F_{850}^{(3)}$ mJy/bm	$I(C^{18}O)^{(4)}$ K km s^{-1}
75	03:28:42.6	31:06:10	NGC 1333	None		153	2.2
76	03:32:17.8	30:49:46	None	No SMM/MM source		1916	1.7
77	03:31:21.0	30:45:28	None	I03282+3035	Bachiller et al. (1994); Motte & André (2001)	892	1.1
78	03:47:41.6	32:51:44	None[5]	B5 IRS1	Motte & André (2001)	424	?
79	03:47:39.1	32:52:18	None[5]	None		335	?
80	03:26:37.6	30:15:24	None	No SMM/MM source		302	0.2
81	03:30:15.5	30:23:43	None	No SMM/MM source		253	0.9
82	03:33:13.1	31:19:51	None	None		219	2.4
83	03:32:48.9	31:09:40	None	None		188	0.3
84	03:32:21.9	31:04:56	None[6]	None		184	0.2
85	03:28:32.5	31:00:53	None	03254+3050	Dent et al. (1998)	177	1.5
86	03:26:30.9	30:32:28	None	None		176	1.5
87	03:32:21.5	31:05:08	None[6]	None		166	0.4
88	03:31:31.6	30:43:32	None	None		165	2.2
89	03:32:25.9	30:59:05	None	None		164	2.2
90	03:45:16.5	32:04:47	None	None		163	0.8
91	03:29:23.3	31:36:08	None	None		154	?

[1] If the core satisfies the cluster membership criterion (Sect. 3) then the cluster name is given here.
[2] References are to the earliest previous detection of the submillimetre source. Full cross-identifications with sources at other wavelengths are non-trivial due to differing beam sizes and are left for a future analysis, but to indicate an obvious likely counterpart (e.g., IRAS), "No SMM/MM source" is marked in the "Name" column instead of "None".
[3] SCUBA 850 μm peak flux (14″ beam).
[4] $C^{18}O$ integrated intensity (1′ beam averaged) at the 850 μm peak. A question mark in this column indicates a SCUBA peak which lies outside the $C^{18}O$ map.
[5] B5 pair.
[6] B1 west pair.